Impact of photocatalyst optical properties on the efficiency of solar photocatalytic reactors rationalized by the concepts of initial rate of photon absorption (IRPA) dimensionless boundary layer of photon absorption and apparent optical thickness

Raúl Acosta-Herazo[a], Miguel Ángel Mueses[b], Fiderman Machuca-Martínez[a*], Gianluca Li Puma[c**]

[a]*GAOX Research Group, School of Chemical Engineering, Universidad del Valle, A.A. 25360 Cali, Colombia*

[b]*Photocatalysis and Solar Photoreactors Engineering, Department of Chemical Engineering, Universidad de Cartagena, A.A. 1382-Postal 195 Cartagena, Colombia*

[c]*Environmental Nanocatalysis & Photoreaction Engineering, Department of Chemical Engineering, Loughborough University, Loughborough LE11 3TU, United Kingdom*

**Corresponding author 1:

Tel: +44 1509 222 510;

Email: g.lipuma@lboro.ac.uk

*Corresponding author 2:

Tel: +57 23312935;

Email: fiderman.machuca@correounivalle.edu.co

1

20   **Abstract**

21   The concepts of "initial rate of photon absorption" (IRPA), "dimensionless boundary layer of photon

22   absorption" and "apparent optical thickness (τ_{app})" are presented to evaluate the radiative transfer

23   phenomena in solar, slurry, planar, photocatalytic reactors. The radiation field produced by

24   suspensions of TiO_2 and goethite, two photocatalysts with profoundly different optical properties used

25   in heterogenous photocatalysis and heterogeneous photo-assisted Fenton reactions, was determined

26   by the six-flux radiation absorption-scattering model coupled to the Henyey-Greenstein scattering

27   phase function (SFM-HG). The concept of IRPA, defined by the differentiation at the local volumetric

28   rate of photon absorption (LVRPA) at the reactor window boundary, is proposed as a new approach

29   to determine the impact of catalyst loading and optical properties on the extinction of light inside a

30   photoreactor. The IRPA showed that the extinction of light follows a second order dependency on the

31   photocatalyst concentration while the impact of the optical properties can be expressed by a decoupled

32   function (Ψ function). The Ψ function increased with photocatalyst concentration and approached a

33   maximum at the same optimal photocatalyst concentration determined from the analysis of the total

34   rate of photon absorption (TRPA) in the reactor. The analysis of TRPA and boundary layer of photon

35   absorption redefined here in dimensionless form, as a function of τ_{app}, determined that the most

36   efficient rate of radiation absorption in solar powered planar reactors occurs at τ_{app}=4.1-4.4, with

37   approximately 10% of the reactor width under darkness. τ_{app} is a similarity dimensionless parameter

38   exclusively derived from the SFM approach, which clusters the effects of photocatalyst loading,

39   reactor dimension and photocatalyst optical properties, providing an ideal parameter for designing

40   and scaling photocatalytic reactors operated with any kind of photocatalytic material.

41   **Keywords:** Radiative transfer; Radiation transport; Photoreactor design; Photoreactor model,

42   Optimization.

43

Nomenclature

a	SFM parameter, dimensionless
b	SFM parameter, dimensionless
C_{cat}	photocatalysts concentration, kg m^{-3}
g	scattering parameter from the Henyey-Greenstein phase function, dimensionless
$IRPA$	initial rate of photon absorption, W m^{-4}
I_0	incident radiative flux, W/m^2
I_λ	spectral irradiance, W m^{-2} nm^{-1}
L	thickness of the photocatalyst-water film, m
LVRPA or e^a	local volumetric rate of photon absorption, W m^{-3}
p_b	SFM probability of scattering in the backward direction, dimensionless
p_f	SFM probability of scattering in the forward direction, dimensionless
p_s	SFM probability of scattering in the sideward direction, dimensionless
$TRPA/A$	total rate of photon absorption per unit of transversal surface of the photoreactor, W m^{-2}
x	x coordinate, m

Greek letters

β^*	extinction coefficient, m^2 kg^{-1}
δ	boundary layer of photon absorption
γ	SFM parameter, dimensionless
κ^*	absorption coefficient, m^2 kg^{-1}
λ	wavelength, nm
σ^*	scattering coefficient, m^2 kg^{-1}
τ	optical thickness, dimensionless
τ_{app}	apparent optical thickness from SFM, dimensionless
ψ	psi function
ω	scattering albedo, dimensionless
ω_{corr}	corrected scattering albedo from SFM, dimensionless

Subscripts

max	maximum
min	minimum
UVA	UVA region of the solar spectrum
Vis	visible region of solar spectrum
max	maximum

44

1.   Introduction

46 Platform technologies such as heterogeneous photocatalysis and the photo-assisted heterogeneous

47 Fenton process have shown great potential for the treatment of contaminated water or air [1,2]. The

48 main attraction of these processes is the utilization of solar light as the driving force for the production

49 of highly oxidative radical species, which are then able to complete the conversion of water or air

50 contaminants to innocuous products.

51

52 One very active field of research in heterogeneous photocatalysis is the development and evaluation

53 of new photocatalytic materials. Doping of commercial titanium dioxide (TiO_2) is a common

54   approach to extend the absorption spectrum of TiO_2 from the UV into the visible region of the solar

55   spectrum [3]. Furthermore, iron oxides, have shown interesting properties as visible light active

56   photocatalyst, as well as, catalysts for photo-assisted heterogeneous Fenton reactions when combined

57   with hydrogen peroxide [4–6].

58

59   The intense development in new photocatalysts calls for the development of comprehensive

60   methodologies for the analysis of the radiative transfer behavior of these new materials, particularly

61   in the solar radiation spectrum. These methodologies are necessary for an appraisal of the catalytic

62   performance of new photocatalytic materials and for the design and optimization of solar

63   photoreactors. For this purpose, the optical properties of existing or new photocatalysts (the

64   extinction, absorption and scattering coefficients and the scattering phase function) must be

65   determined or estimated.

66

67   Recently several authors have investigated the influence of the optical properties on the photocatalyst

68   performance [7–9], however, the literature has scarce information on the application of these for

69   reactor design. Besides, available information deals almost exclusively with TiO_2 P25 photocatalyst.

70   Furthermore, optimized photoreactor designs have been proposed in conjunction with TiO_2

71   photocatalytic powders, however, it remain unclear if these designs are also optimal when the reactor

72   is loaded with other photocatalysts, particularly those materials having highly different optical

73   properties than TiO_2. Process intensification, for instance, is a novel and very interesting approach

74   for optimizing photocatalytical processes [10,11]. One aspect that the intensification process should

75   consider firstly is the optical performance of the photocatalytical material (i.e. its optical properties)

76   for an integral design or correct selection of the photoreactor. In general, the optimization of the

77   reactor performance requires a detailed analysis between the operational parameters such as, optimal

78   photocatalyst loading, which in turn depend on the optical properties of the synthesized material and

79   the rate of absorption of radiation.

4

80   In this study, an alternative reaction engineering approach including the impact of the photocatalyst

81   optical properties on the optimization of photoreactors is presented i.e. in the determination of an

82   optimal catalyst loading or photoreactor size. The concepts of "initial rate of photon absorption"

83   (IRPA) and "boundary layer of photon absorption" [12] redefined in dimensionless form are here

84   proposed as new parameters for evaluating the impact of photocatalyst loading on the total rate of

85   photon radiation absorption (TRPA) and to facilitate the optimal design of photoreactors at different

86   scales, from laboratory scale to full scale. The consequence of these are far reaching since the

87   evaluation of the wide range of photocatalysts reported in literature may have to be reconsidered, if

88   the photocatalysts activity was determined at equal loadings in the reactor without accounting the

89   impact of the photocatalysts optical properties.

90

91   Goethite (α-FeOOH), an iron oxide used as visible-active photocatalysts [13] as well as for photo-

92   assisted heterogeneous Fenton reactions [14,15], and the extensively explored TiO_2 P25 were selected

93   to illustrate the impact of the above methodology on materials with significantly different optical

94   properties. The use of goethite as one of the model photocatalysts also offers an illustration of the

95   evaluation of the radiative transfer phenomena of a photocatalyst active in the visible range of the

96   solar spectrum, which may be the of special interest to the literature. The optical performance of

97   these photocatalysts was evaluated in a simple planar photoreactor geometry, allowing the results and

98   concepts of this study to be easily transferred to other photoreactor geometries. Such geometry is

99   characteristic of falling liquid films [16] and conventional flat-plate photoreactors, with the slurry

100   photocatalyst suspension confined between two walls [17,18]. The six-flux absorption scattering

101   model (SFM) was used to model the solar radiation transport through slurry suspensions of the

102   photocatalysts.

5

2.   Mathematical methods

2.1.   Optical properties of photocatalysts and solar spectral irradiation

The spectral absorption and scattering coefficients of the photocatalysts TiO_2 (P25, Evonik) and goethite (α-FeOOH, Aldrich) in aqueous suspensions [19,20] are shown in **Fig. 1** and **Fig. 2**, including the solar radiation data of global irradiance (AM 1.5), incident on a plane tilted 37° facing the sun [21]. The wavelengths range of 310-500 nm was selected since 300 nm is the lower wavelength in which both the goethite and TiO_2 interact with light and 500 nm is the upper limit for goethite, beyond this value Ortiz de la Plata et al. [20] found that the absorption of radiation by goethite was too small to be taken into account. Similarly, the graphical representation of the Henyey-Greenstein scattering factor is presented in **Fig. S1** (Supporting Information (SI)).
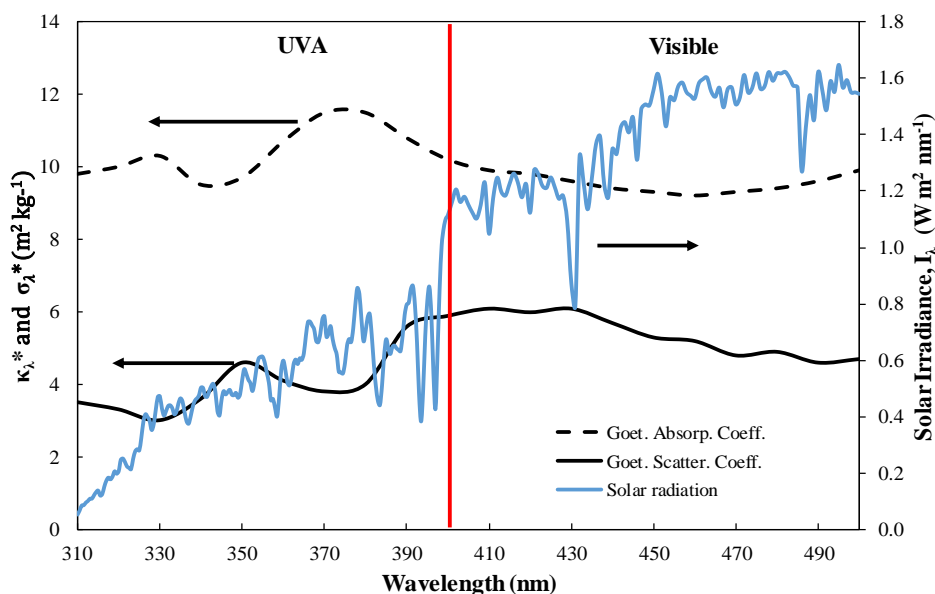
Fig. 1 Optical properties of goethite (Aldrich) and solar irradiance for a surface tilted 37° to the sun. The red line separates the UVA and visible regions of the solar spectrum. Absorption and scattering coefficients from [20].

6

117
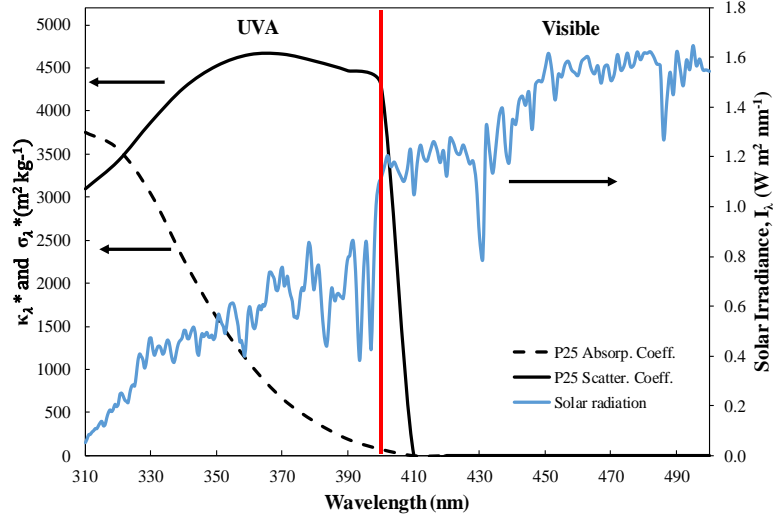
Fig. 2 Optical properties of TiO₂ P25 (Evonik) and solar irradiance for a surface tilted 37° to the sun. The red line separates the UVA and visible regions of the solar spectrum. Absorption and scattering coefficients from [19].

2.2. The Six Flux Model for radiation field calculations

The spatial distribution of the local volumetric rate of photon absorption (LVRPA) inside the planar reactor was evaluated by the SFM as shown in Eq. (1) [22]:

$$e^a(x) = \frac{I_0 \tau_{app}}{\omega_{corr}(1-\gamma)L}\left[\left(\omega_{corr}-1+\sqrt{1-\omega_{corr}^2}\right)e^{-x\tau_{app}/L} + \gamma\left(\omega_{corr}-1-\sqrt{1-\omega_{corr}^2}\right)e^{x\tau_{app}/L}\right] \quad (1)$$

where a, b, ω_{corr} and γ are SFM parameters defined as follows:

$$a = 1-\omega p_f - \frac{4\omega^2 p_s^2}{1-\omega p_f - \omega p_b - 2\omega p_s} \quad (2)$$

$$b = \omega p_b + \frac{4\omega^2 p_s^2}{1-\omega p_f - \omega p_b - 2\omega p_s} \quad (3)$$

$$\omega_{corr} = \frac{b}{a} \quad (4)$$

7

$$\gamma = \frac{1 - \sqrt{1 - \omega_{corr}^2}}{1 + \sqrt{1 - \omega_{corr}^2}} e^{-2\tau_{app}}$$

129 (5)

130 the apparent optical thickness τ_{app} is:

$$\tau_{app} = a\tau\sqrt{1 - \omega_{corr}^2}$$

131 (6)

132 For a planar geometry, the optical thickness τ is defined by:

$$\tau = (\sigma^* + \kappa^*)C_{cat}L$$

133 (7)

134 where σ^* and κ^* are the spectral averaged specific scattering and absorption coefficients, C_{cat} is the

135 photocatalyst loading and L is the characteristic length for the extinction of the light inside the reactor.

136 In this study, the planar reactor is positioned orthogonally to the sun and is irradiated by collimated

137 rays, i.e. L equals the thickness of the depth of the water in the planar reactor (Fig. S2). For such

138 irradiation conditions in planar geometry, SFM has demonstrated its best performance [23].

139 The scattering probabilities p_f, p_b and p_s were determined from the Henyey-Greenstein phase function

140 for each photocatalyst, following the procedure described elsewhere [24].

141 **2.3.   Radiation field modeling approach**

142 The SFM applied to polychromatic radiation sources conveniently uses the spectral averaged optical

143 properties of the photocatalyst. TiO_2 only interacts with light (by absorption or scattering)

144 significantly in the UVA region of the solar spectrum (**Fig. 2**), while goethite absorbs and scatters

145 light in both the UVA and in a portion of the visible region of the solar spectrum (**Fig. 1**). Therefore,

146 the net radiation absorbed by the goethite photocatalyst was calculated summing the contributions

147 from the UVA and the visible regions of the solar spectrum, as shown in [25], also to allow a direct

148 comparison of the two photocatalyst over the UVA region.

8

149   The LVRPA of a TiO$_2$ suspension was therefore, calculated from the contribution from the UVA

150   region,

151
$$e^a{}_{TiO_2}(x) = e^a_{UVA}(x) \tag{8}$$

152   while the net LVRPA of a goethite suspension was calculated summing the two contributions from

153   the UVA and visible regions, as follows:

154
$$e^a{}_{\alpha-FeOOH}(x) = e^a_{UVA}(x) + e^a_{Vis}(x) \tag{9}$$

155   where e^a_{UV} and e^a_{Vis} were determined from Eq. (1) using the specific optical properties of the catalyst

156   averaged over the solar spectrum determined from:

157
$$\kappa^* = \frac{\int_{\lambda_{min}}^{\lambda_{max}} \kappa^*_\lambda I_\lambda d\lambda}{\int_{\lambda_{min}}^{\lambda_{max}} I_\lambda d\lambda} \tag{10}$$

158
$$\sigma^* = \frac{\int_{\lambda_{min}}^{\lambda_{max}} \sigma^*_\lambda I_\lambda d\lambda}{\int_{\lambda_{min}}^{\lambda_{max}} I_\lambda d\lambda} \tag{11}$$

159
$$g = \frac{\int_{\lambda_{min}}^{\lambda_{max}} g_\lambda I_\lambda d\lambda}{\int_{\lambda_{min}}^{\lambda_{max}} I_\lambda d\lambda} \tag{12}$$

160   The integration limits in Eqs. (10-12) in the UVA region where, $\lambda_{min} = 310$ nm and $\lambda_{max} = 400$ nm and

161   in the visible solar spectrum they were, $\lambda_{min} = 400$ nm and $\lambda_{max} = 500$ nm. The use of spectral averaged

9

162 optical properties is a common approach in literature, which allows a considerable reduction in

163 computational time without introducing considerable distortions in the results [26].

164 The UVA solar incident radiation flux on the reactor, I_0 in Eq. (1), was set in $I_{UVA} = 30$ W/m^2. This

165 value corresponds to an experimentally average value of the solar UVA power for a perfectly sunny

166 day around noon on a surface tilted 37° [27], in agreement with the solar spectral irradiance presented

167 in **Fig. 1** and **Fig. 2**. The visible portion of the incident radiation I_{Vis} was computed ensuring a

168 proportional relationship between the solar spectral irradiances in the UVA and the visible regions of

169 the solar spectrum [28]. Therefore, I_{Vis} is given by:

$$170 \quad I_{Vis} = I_{UVA} \frac{\int\limits_{400nm}^{500nm} I_\lambda d\lambda}{\int\limits_{310nm}^{400nm} I_\lambda d\lambda} \quad (13)$$

171 **2.4. The concept of initial rate of photon absorption (IRPA)**

172 The absorption of radiation by the photocatalyst inside the reactor was assumed to be a stationary

173 process [29]. Therefore, in the planar slurry reactor the LVRPA was only a function of the coordinate

174 parallel to the incident rays, denominated as the x-coordinate.

175 The concept of "initial rate of photon absorption" (IRPA) is here proposed as a new significant

176 parameter for the analysis of the radiation absorption in photoreactors. The importance of the IRPA

177 is that it gives insights on the expected trend of the LVRPA over the entire photoreactor. The IRPA

178 is defined in Eq. (14).

$$179 \quad IRPA = -\left[\frac{d}{dx} \left(e^a(x) \right) \right]\Bigg|_{x=0} \quad (14)$$

180 By applying this definition to Eq. (1), the IRPA can be expressed as:

10

181
$$IRPA = -\frac{I_0}{\omega_{corr}(1-\gamma)}\left(\frac{\tau_{app}}{L}\right)^2\left[\gamma\left(\omega_{corr}-1-\sqrt{1-\omega_{corr}^2}\right)-\left(\omega_{corr}-1+\sqrt{1-\omega_{corr}^2}\right)\right] \quad (15)$$

182 By introducing Eq. (6) and (7) in Eq. (15) and by analogy to chemical reactions, the IRPA can be

183 understood as the initial rate of attenuation of the incident photonic energy as results of its

184 "interaction" with the suspended particle of the catalyst. Then, Eq. (15) can be rewritten as:

185
$$IRPA = -I_0 C_{cat}^2 \psi \quad (16)$$

186 where Ψ is given by,

187
$$\psi = (\beta^*)^2 \frac{a^2(1-\omega_{corr}^2)}{\omega_{corr}(1-\gamma)}\left[\gamma\left(\omega_{corr}-1-\sqrt{1-\omega_{corr}^2}\right)-\left(\omega_{corr}-1+\sqrt{1-\omega_{corr}^2}\right)\right] \quad (17)$$

188 where $\beta^* = \sigma^* + \kappa^*$ is the specific extinction coefficient in m²/kg. The psi function Ψ has units in

189 m⁴/kg², C_{cat} in kg/m³ and I_0 in W/m², therefore the IRPA has units in W/m⁴.

190 The mathematical structure of Eq. (16) resembles that of an exponential rate law, generally used to

191 describe the reaction kinetics in conventional chemical reactions. It include three terms: a proportional

192 relationship of the IRPA to the incident radiation I_0, which from its constant nature can be understood

193 as "the reaction rate constant"; a second order term given exclusively by the catalyst's loading C_{cat}

194 and a proportional term represented by the psi function, which relates the optical properties of the

195 catalyst, implicit in the SFM parameters, to the catalyst loading included in the initial rate of photon

196 absorption (IRPA) parameter γ (see Eq. (5)).

197 **2.5. The total rate of photon absorption (TRPA)**

198 The TRPA, which is the overall radiation absorbed within the entire reactor volume [24,30] is a useful

199 parameter to determine the efficiency of photoreactors and the optimal photocatalyst concentration

11

200 to operate the photoreactor. In a planar photoreactor, uniformly irradiated along the x-coordinate, the

201 TRPA per unit surface area is:

$$TRPA / A = \int_0^L e^a(x)dx \qquad (18)$$

2.6. Dimensionless boundary layer of photon absorption for sizing photoreactors

204 The concept of "boundary layer of photon absorption" has recently been introduced as a useful

205 parameter for designing planar-geometry slurry photoreactors [12]. The boundary layer of photon

206 absorption, in analogy to thermal, hydrodynamic and mass boundary layers, is defined as "the reactor

207 thickness measured from the irradiated photoreactor surface, where 99% of total energy is absorbed"

208 [12]. Mathematically it is defined as:

$$\frac{e^a(0) - e^a(\delta_{abs})}{e^a(0) - e^a(L)} = 0.99 \qquad (19)$$

210 The thickness of the boundary layer δ_{abs} for a given photocatalyst is a function of the catalyst loading

211 and the reactor width (L),

$$\delta_{abs} = f(C_{cat}, L) \qquad (20)$$

213 where δ_{abs} has units of length. This concept has been presented for a planar slurry reactor of 1 cm of

214 thickness operated with different commercial TiO_2 powders [12]. This approach, however, is not

215 dependent on reactor thickness and can be easily extended to any reactor size by introducing a

216 dimensionless form of Eq. (20):

$$\delta_{abs}^* = f(\tau) \qquad (21)$$

12

218   with $\delta^*_{abs} = \delta_{abs}/L$ representing the fraction of the reactor width in which 99% of the total energy is

219   absorbed. The optical thickness τ in Eq. (21) is a dimensionless parameter that clusters the effects of

220   the catalyst loading and reactor width L (see Eq. (7)).

221   In order to establish δ^*_{abs} the procedure described by Otálvaro-Marín et al. [12] was followed, by

222   minimizing the objective function Eq. (22) using the Nelder-Mead optimization algorithm:

$$F_{obj}(\delta_{abs}) = \left\{ \left[e^a(0) - e^a(\delta_{abs}) \right] - 0.99 \left[e^a(0) - e^a(L) \right] \right\}^2 \tag{22}$$

224   The solution of Eq. (22) for a given photocatalyst requires the thickness of the reactor L and the

225   catalyst loading C_{cat}. These two parameters are incorporated in the optical thickness. Any combination

226   of L and C_{cat} that leads to the same value of the optical thickness would produce the same result.

227   Therefore, the "dark zone" of a photoreactor, i.e. the portion beyond the which 99% of the incident

228   energy is absorbed, can be easily determined.

229   **3.   Results and discussions**

230   **3.1.   Photocatalysts optical properties and incident solar radiation on the reactor**

231   The visible component of the incident solar radiation on the reactor was determined from Eq. (13),

232    $I_{Vis} = 80.43$ W/m^2, by setting the incident UVA radiation component as $I_{UVA} = 30$ W/m^2. The numerical

233   values of the integrals in Eq. (13) are shown in Table 1. The fraction of solar power between 400-500

234   nm is 2.68 times greater than that for the UVA. Goethite, unlike TiO$_2$ P25, is photoactive between

235   310-500 nm, therefore, it can absorb a significant larger amount of solar energy (18.62% of the

236   complete solar spectrum).

13

237   **Table 1.** Integrated solar irradiance power for regions in analysis.

Region of the solar spectrum	Integrated irradiance power over the wavelength interval (W/m²)	Fraction of total spectrum irradiance power (%)
UVA (310-400 nm)	50.61	5.06
Portion of visible (400-500 nm)	135.70	13.56
Complete spectrum (280-4000 nm)	1000.4[a]	100

238   a. reported in reference [21]

239   The optical properties of the photocatalysts calculated from Eq. (10-12) are reported in Table 2,

240   together with the corresponding values of the scattering albedo and corrected scattering albedo (Eq.

241   (4)). The scattering albedo reported for TiO_2 P25 (0.79) was calculated using the optical properties

242   of sonicated TiO_2 slurries reported by [19] ($\kappa^* = 1144.69$ m²/kg and $\sigma^* = 4397.30$ m²/kg). However,

243   since the optical properties are a function of the grade of agglomeration and hydrodynamics [9,31],

244   which for sonicated suspensions can be 2-4 times greater [32], the correction procedure proposed by

245   Toepfer et al. [33] was adopted. Therefore, the specific scattering and absorption coefficient for TiO_2

246   reported in Table 2 were calculated from $\sigma^* = \beta^* \omega$ and $\kappa^* = \beta^* - \sigma^*$, considering that the specific

247   extinction coefficient of TiO_2 P25 measured under the prevailing conditions of mixing for a solar

248   reactor was $\beta^* = 1470.5$ m²/kg [34]. It is worth to note that the specific extinction coefficient is

249   independent of the scattering phase function adopted.

250   The optical properties of goethite were measured under mixing conditions for a recirculating flow

251   slurry suspension [20].

252   The specific scattering and absorption coefficients of TiO_2 P25 under UVA irradiation (Table 2) were

253   289 and 29 times, respectively, greater than those for goethite, although the scattering albedo of TiO_2

14

254 (i.e., the probability of scattering photons) was significantly higher than the value for goethite. The

255 corrected scattering albedo ω_{corr}, on the other hand, is a correction made to the conventional scattering

256 albedo, and accounts for the scattering phase function. A predominantly backward scattering

257 decreases the probability of absorbing photons while a predominantly forward scattering increases it,

258 since photons will penetrate deeper in the reactor width [24].

259 Goethite has very similar optical coefficients in both visible and UVA regions and very low ω_{corr} as

260 results of its low conventional albedo and a g scattering factor near to 1, indicating a highly

261 predominant forward scattering behavior. Such a low value of ω_{corr} could indicate an efficient

262 exploitation of the incident photons. In addition, in comparison to others visible-active photocatalysts

263 reported in literature (Table S1 (SI)) goethite has a comparable absorption coefficient and the lowest

264 scattering albedo in the visible region of the solar spectrum, which means that goethite has superior

265 capacity for absorbing a high proportion of visible radiation from the solar spectrum.

266 **Table 2.** Optical properties of catalyst.

Photocatalyst	κ^* (m²/kg)	σ^* (m²/kg)	β^* (m²/kg)	g	ω	ω_{corr}
TiO₂ P25[a]	308.8	1161.7	1470.5	0.53	0.79	0.2812
Goethite (UVA region)	10.59	4.32	14.91	0.89	0.29	0.0003
Goethite (Visible region)	9.52	5.28	14.80	0.87	0.36	0.0006

267   a.   Only is considered the UVA region.

268 **3.2.   LVRPA profiles**

269 The LVRPA transversal profiles in a planar reactor of thickness $L = 1$ cm uniformly irradiated on the

270 front surface are shown in **Fig. 3**, for both goethite (Fig. 3a-c) and TiO₂ P25 (Fig. 3d). **Fig. 3**a-c

271 show the LVRPA distribution of goethite considering the UVA (Fig. 3a), the visible portion (Fig. 3b)

272 and the full solar spectrum (Fig. 3c), respectively. The visible component of the LVRPA gives the

15

273　greater contribution to the net LVRPA since the incident radiation I_{Vis} is higher than I_{UVA} and the

274　optical properties of goethite have similar order in both UVA and visible regions. On the other hand,

275　the LVRPA profile of TiO$_2$ P25, under solar irradiation, has on average one order of magnitude higher

276　values, which also agrees with the rigorous solution of the Radiative Transfer Equation (RTE) by the

277　discrete ordinate method [20].
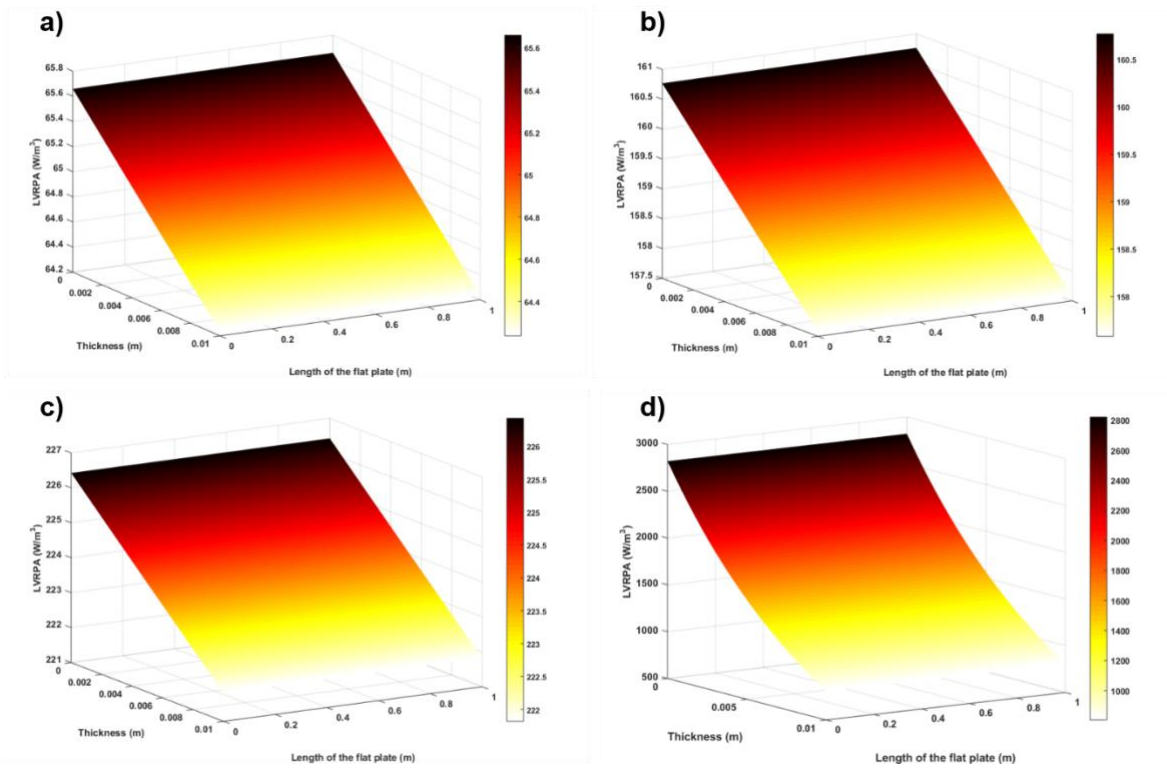
278

279　**Fig. 3** LVRPA spatial distribution on the planar slurry reactor with 0.2 g/L of catalyst. a) Goethite

280　under UVA component of solar radiation b) Goethite under visible component of solar radiation c)

281　Goethite under solar irradiation (UVA + visible components) d) TiO$_2$ P25 under solar irradiation

282　(UVA component).

283　The distribution of the LVRPA in the reactor with both catalysts at different catalyst loading is shown

284　in Fig. 4. The LVRPA gradients for TiO$_2$ increased significantly when the catalyst loading varied

285　from 0.1 to 2.0 g/L. At high catalyst loading, very high LVRPA values are reached near the

286　illuminated boundary of the reactor and a very steep fall results at greater reactor depths. This

16

287 behavior is attributed to the relatively high value of scattering albedo of TiO_2 as discussed elsewhere

288 [35].

289 In sharp contrast to the results shown for TiO_2, goethite displayed an almost uniform distribution of

290 the LVRPA across the reactor depth at all catalyst loading investigated. The gradients of the profiles

291 were considerably less sensitive to the catalyst dosage, which resulted from the significantly lower

292 values of scattering albedos of goethite, which favored the penetration of photons to greater depths

293 in the reactor, compounded with the higher value of forward radiation scattering (g scattering factor

294 near to 1).

295 The impact of the scattering phase function on the distribution of the LVRPA can be significant. In

296 this study, the SFM was coupled to the HG scattering phase function model and both catalysts

297 exhibited primarily forward scattering behavior. Therefore, the penetration of photons down the

298 reactor width and the photon absorption efficiency was favored in comparison to other situations. If

299 the SFM is coupled to the diffuse reflectance phase function, which has a predominantly back

300 scattering behavior, the LVRPA at the illuminated boundary would be approximately 2.15 higher

301 than in this study, however, the overall photon absorption efficiency of the reactor would be lower

302 since a higher fraction of photons would escape from the front wall of the reactor [12]. It should be

303 noted that the HG scattering phase function adopted herein has been recently validated as more

304 reliable than the diffuse reflectance phase function for modeling the radiation field of TiO_2 aqueous

305 suspensions [36].

306

17

307
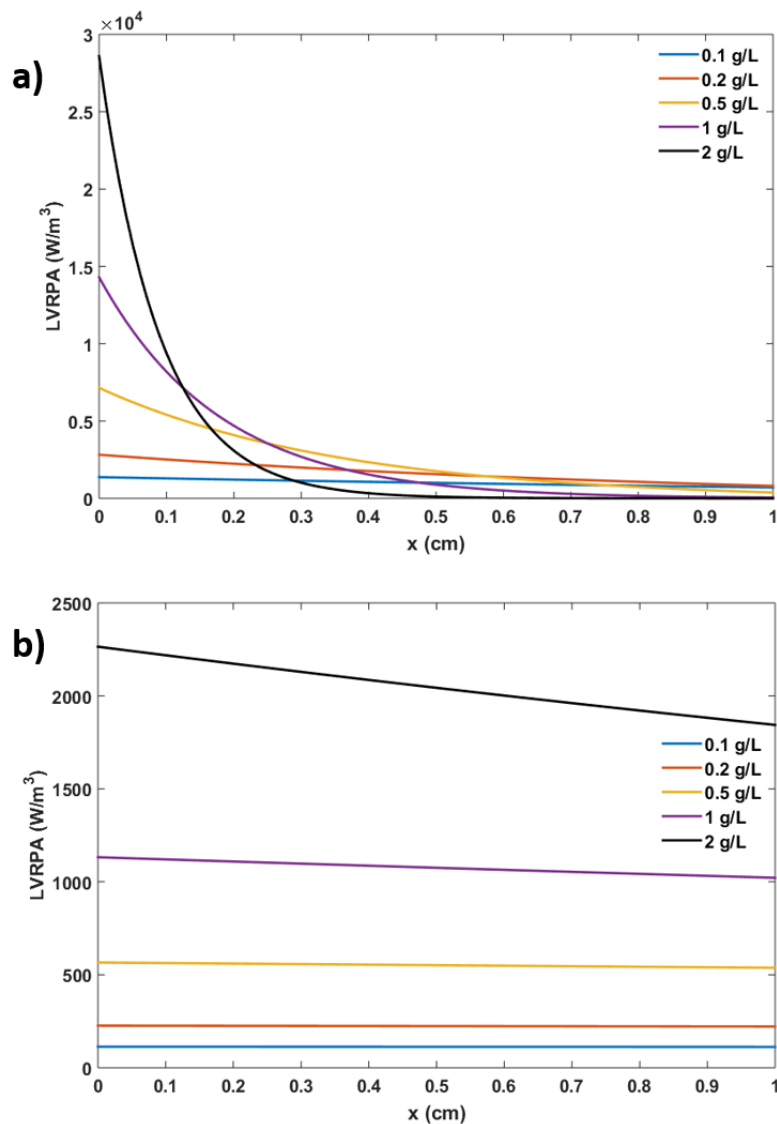
Fig. 4 LVRPA spatial distribution as function of catalyst loading under solar irradiation. a) TiO$_2$ b)

goethite

3.3.   Impact of catalyst loading on the initial rate of photon absorption (IRPA)

Fig. 5 and **Fig. 6** show the behavior of the IRPA (Eqs. 16-17) and the squared of the catalyst loading,

as function of catalysts loading of TiO$_2$ and goethite, respectively. In both cases, the IRPA curve

(black line) almost overlap the square of catalyst loading (red line). The quadratic nature of the IRPA

(Eq. 16) implies a strong dependence from the catalyst loading, in consequence increasing the catalyst

18

315   loading produces significantly steeper decays of the LVRPA profiles. Equivalent IRPA values for

316   TiO_2 and goethite were reached at significantly lower catalyst loadings of the former (**Fig. 5** and **Fig.**

317   **6**) and as a result, stronger gradients of the LVRPA were observed with TiO_2 (**Fig. 4**) at increasing

318   catalyst loadings, while such dependence was weak with goethite. Such a difference also results since

319   TiO_2 has a specific extinction coefficient 98 times higher than goethite.
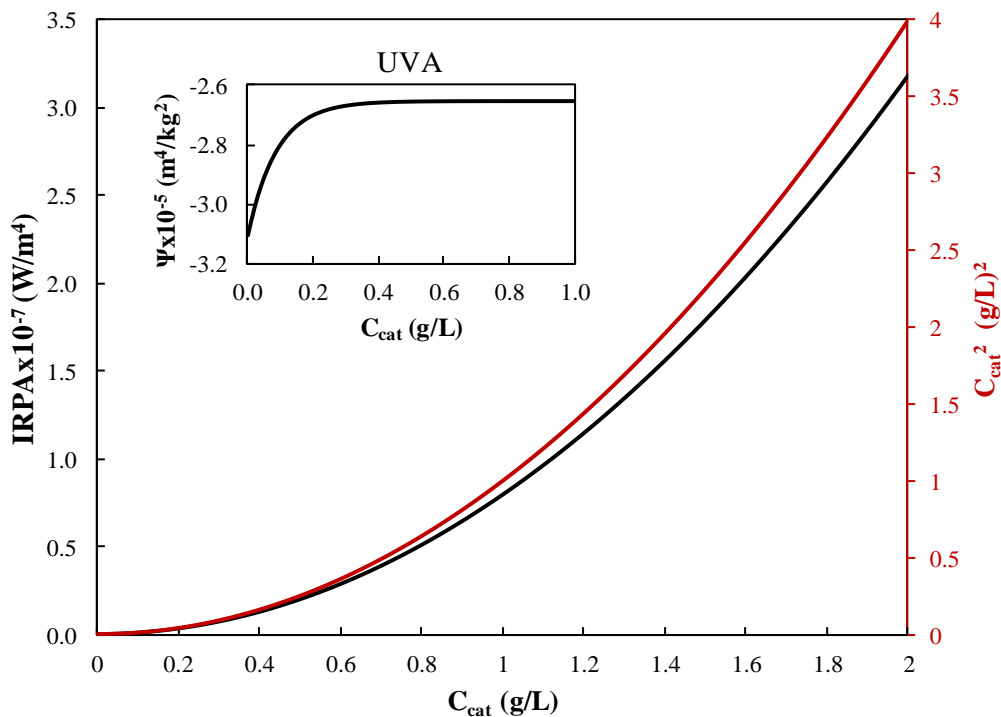
320

321   **Fig. 5** Initial rate of photon absorption as function of catalyst load for TiO_2 P25 for a planar reactor

322   under solar radiation (in black) and the squared catalyst load (in red). The inset figure corresponds to

323   the psi function of Eq. (17).
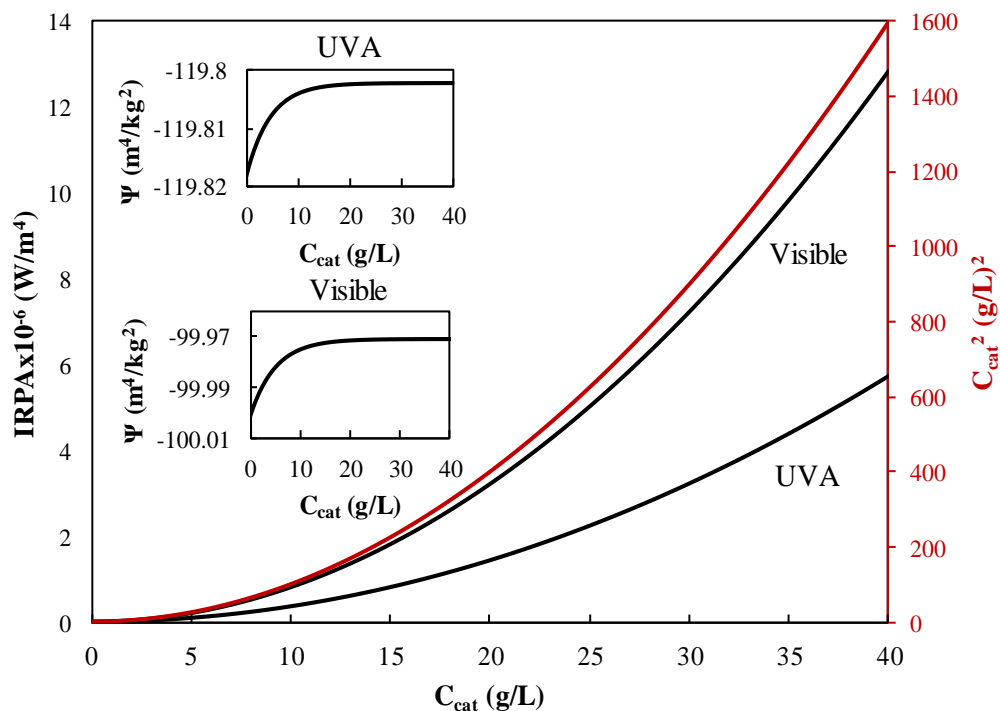
Fig. 6 Initial rate of photon absorption as function of catalyst load for goethite (Aldrich) for a planar reactor (in black) and the squared catalyst load (in red). The inset figures correspond to the psi function of Eq. (17).

Despite the quadratic dependence of the IRPA on the photocatalyst concentration, the behavior of the Ψ function and its impact on the IRPA is worth of further observations. Table S2 (Supporting Information) shows the fitting of a quadratic equation to initial portions of the IRPA profiles of TiO_2 and goethite. In all three cases, a displacement in the y-intercept of the IRPA curve from zero can be observed, which results from the influence of the Ψ function. The impact of the Ψ function reduces at increasing catalyst loading as shown in the inset figures in **Fig. 5** and **Fig. 6** until it reaches a plateau at determined values of C_{cat} in both catalysts. The analytical form of such equation can be predicted analytically taking the limits $C_{cat} \rightarrow 0$ and $C_{cat} \rightarrow \infty$.

Eq. (17) at $C_{cat} \rightarrow 0$ reduces to the equation of a straight line with m as its slope and c as the y-intercept:

20

$$338 \qquad \qquad \qquad \qquad \qquad \Psi = m\gamma + c \qquad \qquad \qquad \qquad \qquad (23)$$

339   with

$$340 \qquad \qquad m = (\beta^*)^2 \frac{a^2(1-\omega_{corr}^2)}{\omega_{corr}}\left(\omega_{corr} - 1 - \sqrt{1-\omega_{corr}^2}\right) \qquad (24)$$

$$341 \qquad \qquad c = -(\beta^*)^2 \frac{a^2(1-\omega_{corr}^2)}{\omega_{corr}}\left(\omega_{corr} - 1 + \sqrt{1-\omega_{corr}^2}\right) \qquad (25)$$

342   where it has been considered $1 \gg \gamma$ and then $(1 - \gamma) \to 1$. This approximation is based on the

343   consideration that the highest value possible for γ occurs when $C_{cat} = 0$ which reduces Eq. (5) to

344    $\gamma = (1-\sqrt{1-\omega_{corr}^2})/(1+\sqrt{1-\omega_{corr}^2})$. For instance, at $C_{cat} = 0$, γ equals 0.04 for TiO$_2$ P25 and 4 $\times$

345   10^{-8} for goethite.

346   On the other hand, at high catalyst loading (i.e. $C_{cat} \to \infty$), $\gamma \to 0$, thus Eq. (23) reduces to:

$$347 \qquad \qquad \qquad \qquad \qquad \psi = c \qquad \qquad \qquad \qquad \qquad (26)$$

348   The Ψ function predicted by Eq. (23) and Eq. (26) is the specular reflection of the curve for catalyst

349   loading shown in the insets of **Fig. 5** and **Fig. 6**, since γ is inversely proportional to C_{cat}.

350   Hence, at low catalyst loadings it can be concluded that the attenuation of the LVRPA in a

351   photoreactor, as shown by the IRPA, has a squared contribution from the catalyst loading and a linear

352   dependence from the photocatalyst optical properties, included in the Ψ function. The Ψ function

353   expresses in a decoupled term, the capability of the photocatalyst to absorbs and to scatter radiation,

354   which are a function of the catalyst optical properties.

355   At low catalyst concentration, the contributions of both catalyst concentration and photocatalyst

356   optical properties are relevant on the IRPA, nonetheless at high catalyst loading the IRPA reduces to:

21

357
$$IRPA = -k_0 C_{cat}^2 \qquad (27)$$

358   where $k_0 = I_0 c$. At high catalyst loading, the photocatalyst optical properties have a less significant

359   impact on the IRPA and the attenuation of LVRPA with reactor depth is governed by the value of the

360   specific extinction coefficient β^* only and by the concentration of solids. In addition, the fraction of

361   photons escaping from the front wall (the illuminated boundary) of the photoreactor increases and γ

362   = 0. The analytical behavior of the Ψ function at high and low photocatalyst loading is also supported

363   by experimental observations. Brandi et al. [37] determined that the back-scattered radiation (the

364   photon flux escaping from the illuminated boundary of the reactor) was a linear function of the

365   catalyst concentration at low catalyst loading (below the reported optimal value) and beyond the

366   optimum (once the absorption of radiation in the reactor reached a plateau) the back-scattered

367   radiation became independent from the concentration of solids [37].

368   **3.4.   Optimization of rate of photon absorption in planar slurry photoreactors**

369   The optimization of the rate of photon absorption in photoreactors can be accomplished by

370   maximizing the TRPA (Eq. 18) as a function of the photocatalyst loading. The total rate of photon

371   absorption per unit of surface area (TRPA / A) in the planar photoreactor was therefore calculated by

372   integrating the LVRPA across the photoreactor width. The TRPA/A as function of the photocatalyst

373   dosage and apparent optical thickness, τ_{app}, in a 1 cm planar slurry reactor irradiated by solar light is

374   shown in **Fig. 7**a-c. The TRPA/A increases with photocatalyst loading for both photocatalysts

375   approaching plateaus. The concentration of photocatalyst corresponding to TRPA/A changing less

376   than 0.5% can be considered an optimum. Such optimum for TiO_2 is approximately at 0.75 g/L

377   corresponding to an apparent optical thickness of 4.17, which lays within the optimum range reported

378   for planar reactors (τ_{app} = 1.8 - 4.4) [38]. The adoption of the scattering phase function may have a

379   significant effect on the optimum catalyst concentration that maximize the rate of photon absorption.

380   In fact, coupling the SFM to the diffuse reflectance phase function resulted to an optimum TRPA for

22

381   TiO$_2$ at 0.2 g/L, for the same reactor thickness ($L = 1$ cm) [12]. Since the diffuse reflectance phase

382   function favors predominantly backward scattering, sharper LVRPA gradients and diminished

383   penetration of photons across the reactor depth would be expected, therefore the optimum catalyst

384   concentration that maximize the rate of photon absorption occurs at lower values. The higher

385   optimum catalyst loading predicted in this study resulted from the predominant forward scattering

386   phase function (Table 2, g-values). The optimum catalyst concentration reported here agrees with

387   experimental and modeling results by Camera-Roda et al. [39], who reported 0.75 g/L for a planar

388   reactor illuminated with LEDs. This corresponds to $\tau_{app} = 3.91$, which is very close to the value

389   reported in this study.

390   In sharp contrast, the TRPA with goethite catalyst reached an optimum at significantly higher catalyst

391   concentrations ($C_{cat} \approx 40$ g/L, $\tau_{app} = 4.37$) (**Fig. 7**b), which results from the very low value of the

392   specific extinction coefficient of goethite. Clearly, such value of catalyst loading is not viable in

393   practical application, and further considerations must be done by including the effect of particle

394   agglomeration and hydrodynamics on nanoparticle optical properties as discussed elsewhere [40,41].

395   However, goethite can reach TRPA / A of similar order to the maximum value observed with TiO$_2$,

396   at catalyst concentrations in the range 2 - 3 g/L (**Fig. 7**b) since goethite can absorb a significant

397   amount of visible light. Clearly, the results shown in **Fig. 7**b show that very high goethite

398   concentrations are necessary to reach limitations in the transfer of radiant energy, if only the effect of

399   optical properties were considered. However, in practice optimum catalyst loading may have to be

400   considered including other considerations such as expected reaction kinetics, slurry handling,

401   mechanical and hydrodynamics limitations.

402   The evaluation of the optimum catalyst loading in photoreactors has been the subject of many

403   experimental and modeling studies. It is well known that the TRPA follows an initial linear

404   dependence with the catalyst loading and that excessive loading results in a plateau. This effect has

405   been qualitatively described by some as "the photocatalyst clouding effect" in experimental studies

23

406   [42]. In reality, such clouding effect can be rationalized by a simple numerical parameter, which is

407   the apparent optical thickness, τ_{app} (Eq. (6)). τ_{app} is a similarity dimensionless parameter, which in its

408   definition clusters the effects of catalyst loading, reactor dimension and catalyst optical properties,

409   allowing a comparison between photocatalytic systems with similar geometries. The optimum values

410   for the apparent optical thickness are only function of the reactor geometry and the hydrodynamic

411   conditions in the reactor, and typical optimum ranges have been reported in literature for both planar

412   and tubular photoreactors [38,43]. The proximity of the values of the apparent optical thicknesses in

413   which the TRPA approaches a plateau with both goethite and TiO_2 (Fig. 7c) is, therefore, not a casual

414   coincidence.

415   The behavior of the TRPA/A as function of the catalyst loading observed in **Fig. 7**a-b is similar to

416   that observed for the Ψ function (insets plots in **Fig. 5** and **Fig. 6**). The initial linear dependence with

417   catalyst loading varies until it reaches a plateau. The value in which Ψ reaches a constant value ($\Psi =$

418   c) approaches the optimum catalyst loadings for TiO_2 (0.75 g/L) and goethite (40 g/L), which suggest

419   the existence of a direct relationship between the behavior shown by the Ψ function and the TRPA.

420   Therefore, by similarity to Ψ it can be concluded that the TRPA initially increases linearly with

421   respect to the catalyst concentration, since both absorption of radiation and forward photon scattering

422   are controlling factors of the radiation transport. However, as the catalyst loading and the opacity of

423   the reactor increases, the impact of forward photon scattering becomes less significant, since the

424   photons have a reduced ability to penetrate through the reactor width. Therefore, photon absorption

425   becomes predominant to the transport of radiation through the reactor, back-scattering become

426   significant allowing a higher fraction of photon loss from the reactor front window and the TRPA

427   reaches a plateau with the catalyst loading.

428   It can be concluded that the Ψ function is an analytical representation of the behavior of the TRPA as

429   a function of the catalyst loading in photoreactors. This represents a new simple way for visualizing

24

430   the radiation field in a photocatalytic reactor and for determining optimum catalyst loading, even in

431   non-planar photoreactor geometries (e.g., cylindrical).

432
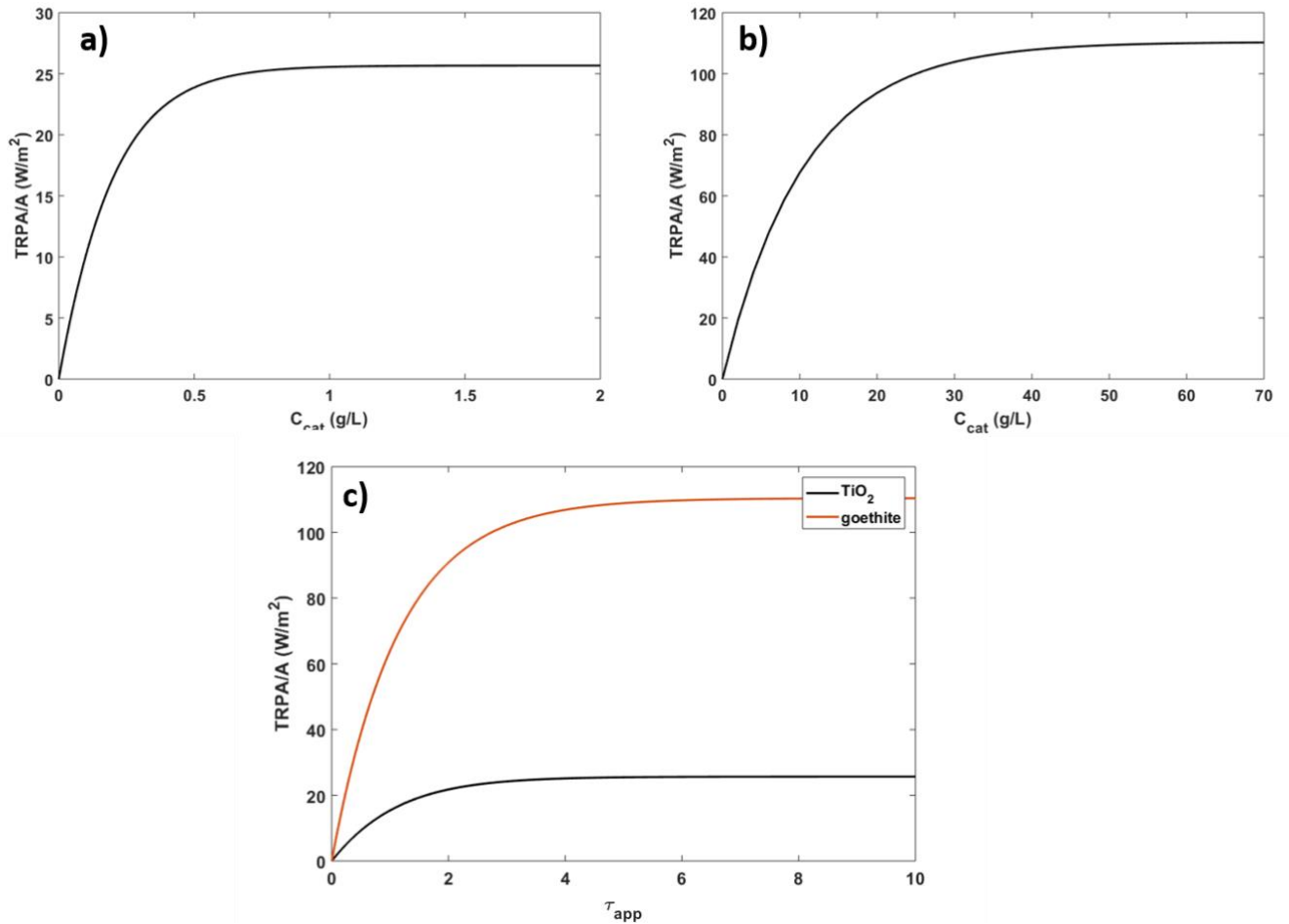
433

434   **Fig. 7** TRPA per unit of surface area in a planar slurry reactor of thickness $L = 1$ cm irradiated by

435   solar light as function of catalyst loading. a) TiO_2 P25 b) goethite and c) TRPA per unit of surface

436   area as function of apparent optical thickness for TiO_2 P25 and goethite.

437   **3.5.**   **Dimensionless boundary layer of photon absorption and its impact on reactor design**

438   Considering a photocatalyst and its optical properties (σ_λ^*, κ_λ^* and g_λ) or more conveniently the

439   corresponding spectral averages (Eqs. 10-12), the conceptual design of a planar photoreactor requires

25

440   the determination of an adequate reactor thickness (L) and an optimal catalyst loading, ($C_{cat,\ opt}$) that

441   maximizes the absorption of the incident radiation. These two design parameters are correlated by the

442   dimensionless parameters: optical thickness τ and apparent optical thickness τ_{app}. These are similarity

443   parameters, since two reactors operated at the same value of τ or τ_{app} will performed similarly in terms

444   of absorption of radiation, independently of photocatalyst loading or reactor dimensions.

445   **Fig. 8** presents the TRPA and the dimensionless boundary layer thickness defined in Eq. (21)

446   calculated by the solution of Eq. (22) for both TiO_2 and goethite photocatalysts, as function of the

447   optical thickness. The optimum optical thicknesses for TiO_2 and goethite are rather different, $\tau_{opt} =$

448   12.18 and $\tau_{opt} = 6.25$, respectively, while the corresponding apparent optical thicknesses are very

449   similar ($\tau_{app,opt} = 4.17$ and $\tau_{app,opt} = 4.37$ for TiO_2 and goethite) in accordance to the results in Fig. 7c.

450   The dimensionless boundary layer, under the conditions of optimum optical thickness, are $\delta^* = 0.86$

451   and $\delta^* = 0.89$ for TiO_2 and goethite respectively, which implies that approximately 14% and a 11%

452   of the reactor width can be considered under darkness, respectively.

26

453
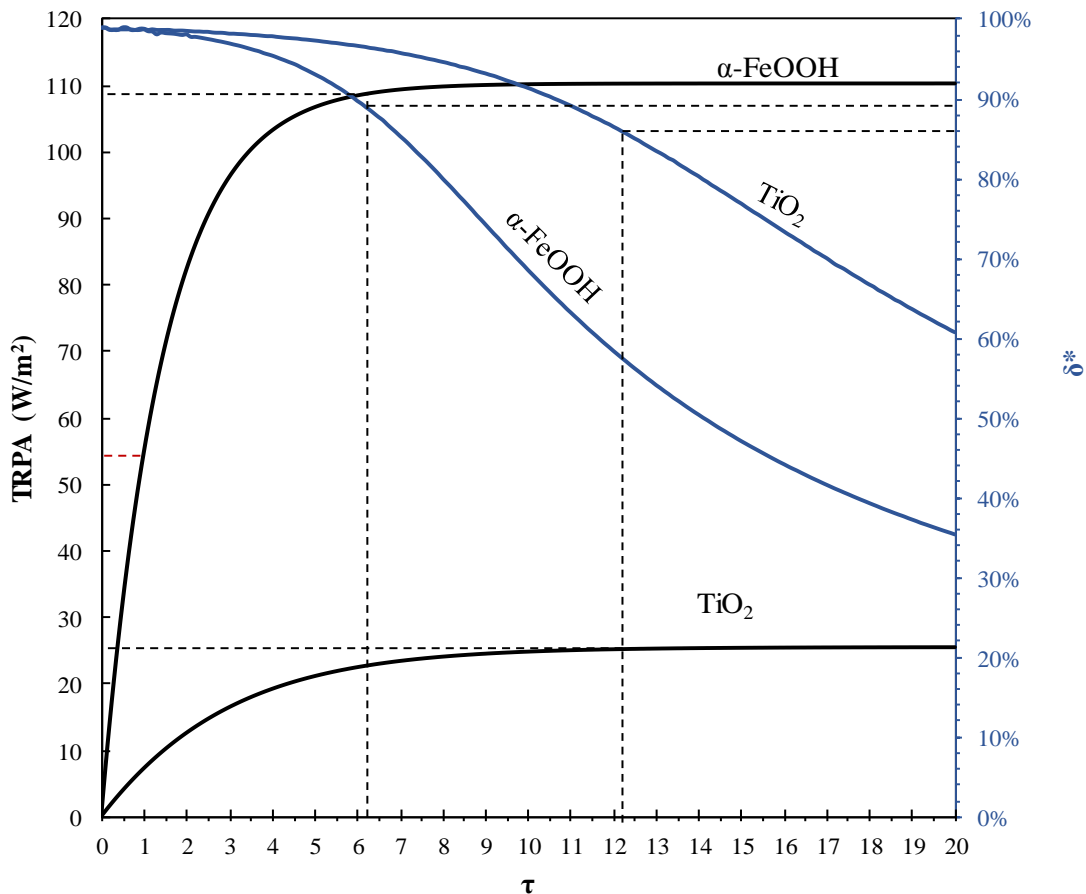
Fig. 8 TRPA (in black) and dimensionless boundary layer of photon absorption as function of the optical thickness of the reactor (in blue). Black dotted lines indicate the TRPA and δ^* for the optimum optical thickness τ for both catalyst.

Plotting the dimensionless boundary layer as a function of the apparent optical thickness, τ_{app}, instead of the conventional optical thickness, τ, produces one single line irrespective of the photocatalyst optical properties (Fig. 9) (i.e. the blue lines in Fig. 8 overlap). It shows that under optimal conditions for radiation absorption ($\tau_{app} = 4.1$ - 4.4) around 10% of the reactor width will be under darkness. The use of the apparent optical thickness goes beyond the limitations imposed by the use of conventional optical thickness (τ), since τ_{app} is insensitive to the photocatalysts optical properties providing an

463   ideal similarity parameter for designing and scaling solar photocatalytic reactors with whatever

464   photocatalyst. Particle agglomeration usually observed at very high catalyst concentrations can have

465   a strong impact on the photocatalyst optical properties [40,41] on the optical thickness (τ) and on the

466   optimal design of thin-film photoreactors, but the range of apparent optical thickness (τ_{app}) that would

467   produce an optimum design remain unaffected.

468
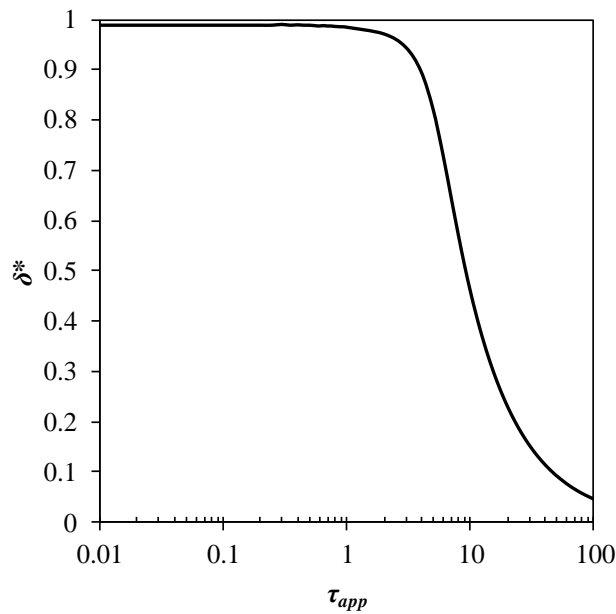
469

470   **Fig. 9** Dimensionless boundary layer of photon absorption as function of the apparent optical

471   thickness.

472   **4.   Conclusions**

473   In this study, a simple and comprehensive reaction engineering approach based on the radiative

474   transfer properties of photocatalysts was presented for evaluating, designing and scaling solar planar

475   photocatalytic reactors. The spatial distribution of the radiation field along the reactor was evaluated

476   by the six-flux radiation absorption-scattering model with the Henyey-Greenstein scattering phase

28

477   function considering irradiation by the solar spectrum. Using the SFM approach, the novel concepts

478   of the "initial rate of photon absorption" (IRPA) and "boundary layer of photon absorption" redefined

479   in dimensionless form together with the apparent optical thickness were introduced and combined in

480   order to obtain an alternative basis for photoreactor optimization.

481   The IRPA allowed a suitable mathematical analysis for determining the impact of catalyst loading

482   and optical properties on the extinction of light inside the photoreactor offering a new way for

483   understanding the radiative transfer phenomena. The IRPA showed that the extinction of light follows

484   a second order dependency from the photocatalyst concentration with the impact of the optical

485   properties expressed by a decoupled term. The common optimization approach that determines the

486   catalyst loading that maximizes the total rate of photon absorption in photoreactors, was

487   complemented with the concept of dimensionless boundary layer of photon absorption, which

488   allowed the determination of the fraction of the reactor under darkness, i.e. not useful for a

489   photocatalytic reaction. The optimum reported in terms of catalyst loading is a strong function of the

490   optical properties of the photocatalysts, which indicates that comparing the performance of

491   photocatalysts having different optical properties at the same catalyst loading may be inconclusive.

492   The previous concepts when analyzed as function of the apparent optical thickness, which is

493   insensitive to the photocatalyst optical properties, allow some important generalizations. The

494   optimum range for radiation absorption in a planar photoreactor should be determined at (τ_{app} = 4.1 -

495   4.4) with a fraction of darkness for the reactor width determined from the dimensionless boundary

496   layer of photon absorption of approximately 10%, these results being valid for any photocatalyst. The

497   apparent optical thickness is, therefore, the ideal similarity parameter for designing and scaling

498   photocatalytic slurry reactors.

499   Finally, it should be highlighted that studies reported in literature comparing the activity of

500   synthesized photocatalytic materials in a slurry suspension, using the same catalyst concentration,

501   may be adversely affected by the differences in the rate of photon absorption, particularly if the

29

502 materials present different optical properties. In consequence, some of the conclusions given may

503 need to be revisited.

509 **References**

510 [1] C. Byrne, G. Subramanian, S.C. Pillai, Recent advances in photocatalysis for environmental

511   applications, J. Environ. Chem. Eng. (2017). doi:10.1016/j.jece.2017.07.080.

512 [2] N. Wang, T. Zheng, G. Zhang, P. Wang, A review on Fenton-like processes for organic

513   wastewater   treatment,   J.   Environ.   Chem.   Eng.   4   (2016)   762–787.

514   doi:10.1016/j.jece.2015.12.016.

515 [3] R. Fagan, D.E. McCormack, D.D. Dionysiou, S.C. Pillai, A review of solar and visible light

516   active TiO_2 photocatalysis for treating bacteria, cyanotoxins and contaminants of emerging

517   concern, Mater. Sci. Semicond. Process. 42 (2016) 2–14. doi:10.1016/j.mssp.2015.07.052.

518 [4] S. Giannakis, S. Liu, A. Carratalà, S. Rtimi, M. Talebi Amiri, M. Bensimon, C. Pulgarin, Iron

519   oxide-mediated semiconductor photocatalysis vs. heterogeneous photo-Fenton treatment of

520   viruses in wastewater. Impact of the oxide particle size., J. Hazard. Mater. 339 (2017) 223–

521   231. doi:10.1016/j.jhazmat.2017.06.037.

522 [5] C. Cai, Z. Zhang, J. Liu, N. Shan, H. Zhang, D.D. Dionysiou, Visible light-assisted

523   heterogeneous Fenton with $ZnFe_2O_4$ for the degradation of Orange II in water, Appl. Catal. B

30

524   Environ. 182 (2016) 456–468. doi:10.1016/j.apcatb.2015.09.056.

525   [6]   R.S. Jack, G.A. Ayoko, M.O. Adebajo, R.L. Frost, A review of iron species for visible-light

526   photocatalytic water purification, Environ. Sci. Pollut. Res. 22 (2015) 7439–7449.

527   doi:10.1007/s11356-015-4346-5.

528   [7]   A. Tolosana-Moranchel, J.A. Casas, J. Carbajo, M. Faraldos, A. Bahamonde, Influence of

529   TiO_2 optical parameters in a slurry photocatalytic reactor: Kinetic modelling, Appl. Catal. B

530   Environ. 200 (2017) 164–173. doi:10.1016/j.apcatb.2016.06.063.

531   [8]   J. Carbajo, A. Tolosana-Moranchel, J.A. Casas, M. Faraldos, A. Bahamonde, Analysis of

532   photoefficiency in TiO_2 aqueous suspensions: Effect of titania hydrodynamic particle size and

533   catalyst loading on their optical properties, Appl. Catal. B Environ. 221 (2018) 1–8.

534   doi:10.1016/j.apcatb.2017.08.032.

535   [9]   A. Turolla, D. Santoro, J.R. de Bruyn, F. Crapulli, M. Antonelli, Nanoparticle scattering

536   characterization and mechanistic modelling of UV-TiO_2 photocatalytic reactors using

537   computational fluid dynamics, Water Res. 88 (2016) 117–126.

538   doi:10.1016/j.watres.2015.09.039.

539 [10]   B.A. Marinho, R.O. Cristóvão, R. Djellabi, A. Caseiro, S.M. Miranda, J.M. Loureiro, R.A.R.

540   Boaventura, M.M. Dias, J.C.B. Lopes, V.J.P. Vilar, Strategies to reduce mass and photons

541   transfer limitations in heterogeneous photocatalytic processes: Hexavalent chromium

542   reduction studies, J. Environ. Manage. 217 (2018) 555–564.

543   doi:10.1016/j.jenvman.2018.04.003.

544 [11]   A.M. Díez, F.C. Moreira, B.A. Marinho, J.C.A. Espíndola, L.O. Paulista, M.A. Sanromán, M.

545   Pazos, R.A.R. Boaventura, V.J.P. Vilar, A step forward in heterogeneous photocatalysis:

546   Process intensification by using a static mixer as catalyst support, Chem. Eng. J. 343 (2018)

547   597–606. doi:10.1016/j.cej.2018.03.041.

548 [12] H.L. Otálvaro-Marín, M.A. Mueses, F. Machuca-Martínez, Boundary layer of photon

549   absorption applied to heterogeneous photocatalytic solar flat plate reactor design, Int. J.

550   Photoenergy. 2014 (2014) 1–8. doi:10.1155/2014/930439.

551 [13] M. el mehdi Benacherine, N. Debbache, I. Ghoul, Y. Mameri, Heterogeneous photoinduced

552   degradation of amoxicillin by Goethite under artificial and natural irradiation, J. Photochem.

553   Photobiol. A Chem. 335 (2017) 70–77. doi:10.1016/j.jphotochem.2016.11.008.

554 [14] Y. Wang, J. Fang, J.C. Crittenden, C. Shen, Novel RGO/α-FeOOH supported catalyst for

555   Fenton oxidation of phenol at a wide pH range using solar-light-driven irradiation, J. Hazard.

556   Mater. 329 (2017) 321–329. doi:10.1016/j.jhazmat.2017.01.041.

557 [15] Y. Liu, X. Liu, Y. Zhao, D.D. Dionysiou, Aligned α-FeOOH nanorods anchored on a graphene

558   oxide-carbon nanotubes aerogel can serve as an effective Fenton-like oxidation catalyst, Appl.

559   Catal. B Environ. 213 (2017) 74–86. doi:10.1016/j.apcatb.2017.05.019.

560 [16] J. Saien, A.R. Soleymani, Feasibility of using a slurry falling film photo-reactor for individual

561   and   hybridized   AOPs,   J.   Ind.   Eng.   Chem.   18   (2012)   1683–1688.

562   doi:10.1016/j.jiec.2012.03.014.

563 [17] G. Di Capua, N. Femia, M. Migliaro, O. Sacco, D. Sannino, K. Stoyka, V. Vaiano,

564   Intensification of a flat-plate photocatalytic reactor performances by innovative visible light

565   modulation techniques: A proof of concept, Chem. Eng. Process. Process Intensif. 118 (2017)

566   117–123. doi:10.1016/j.cep.2017.05.004.

567 [18] M.L. Satuf, R.J. Brandi, A.E. Cassano, O.M. Alfano, Scaling-up of slurry reactors for the

568   photocatalytic degradation of 4-chlorophenol, Catal. Today. 129 (2007) 110–117.

569   doi:10.1016/j.cattod.2007.06.056.

570 [19] M.L. Satuf, R.J. Brandi, A.E. Cassano, O.M. Alfano, Experimental method to evaluate the

32

571   optical properties of aqueous titanium dioxide suspensions, Ind. Eng. Chem. Res. 44 (2005)

572   6643–6649. doi:10.1021/ie050365y.

573   [20] G.B. Ortiz de la Plata, O.M. Alfano, A.E. Cassano, Optical properties of goethite catalyst for

574   heterogeneous photo-Fenton reactions. Comparison with a titanium dioxide catalyst, Chem.

575   Eng. J. 137 (2008) 396–410. doi:10.1016/j.cej.2007.05.008.

576   [21] ASTM, Standard Tables for Reference Solar Spectral Irradiances : Direct Normal and

577   Hemispherical on 37° Tilted Surface, ASTM. G173-03 (2013) 1–21. doi:10.1520/G0173-

578   03R12.2.

579   [22] A. Brucato, A.E. Cassano, F. Grisafi, G. Montante, L. Rizzuti, G. Vella, Estimating radiant

580   fields in flat heterogeneous photoreactors by the six-flux model, AIChE J. 52 (2006) 3882–

581   3890. doi:10.1002/aic.10984.

582   [23] M.A. Ramírez-Cabrera, P.J. Valadés-Pelayo, C.A. Arancibia-Bulnes, E. Ramos, Validity of

583   the Six-Flux model for photoreactors, Chem. Eng. J. 330 (2017) 272–280.

584   doi:10.1016/j.cej.2017.07.120.

585   [24] R. Acosta-Herazo, J. Monterroza-Romero, M.Á. Mueses, F. Machuca-Martínez, G. Li Puma,

586   Coupling the Six Flux Absorption-Scattering Model to the Henyey-Greenstein scattering

587   phase function: Evaluation and optimization of radiation absorption in solar heterogeneous

588   photoreactors, Chem. Eng. J. 302 (2016) 86–96. doi:10.1016/j.cej.2016.04.127.

589   [25] I. Grčić, G. Li Puma, Six-flux absorption-scattering models for photocatalysis under wide-

590   spectrum irradiation sources in annular and flat reactors using catalysts with different optical

591   properties, Appl. Catal. B Environ. 211 (2017) 222–234. doi:10.1016/j.apcatb.2017.04.014.

592   [26] R.L. Romero, O.M. Alfano, A.E. Cassano, Cylindrical photocatalytic reactors. Radiation

593   absorption and scattering effects produced by suspended fine particles in an annular space,

594   Ind. Eng. Chem. Res. 36 (1997) 3094–3109. doi:10.1021/ie960664a.

595   [27] S. Malato, J. Blanco, A. Vidal, P. Fernández, J. Cáceres, P. Trincado, J.C. Oliveira, M.

596   Vincent, New large solar photocatalytic plant: Set-up and preliminary results, Chemosphere.

597   47 (2002) 235–240. doi:10.1016/S0045-6535(01)00220-X.

598   [28] G. Li Puma, P.L. Yue, A laminar falling film slurry photocatalytic reactor. Part II—

599   experimental validation of the model, Chem. Eng. Sci. 53 (1998) 3007–3021.

600   doi:10.1016/S0009-2509(98)00120-1.

601   [29] A.E. Cassano, O.M. Alfano, Reaction engineering of suspended solid heterogeneous

602   photocatalytic reactors, Catal. Today. 58 (2000) 167–197. doi:10.1016/S0920-

603   5861(00)00251-0.

604   [30] P.J. Valadés-Pelayo, J. Moreira del Rio, P. Solano-Flores, B. Serrano, H. de Lasa, Establishing

605   photon absorption fields in a Photo-CREC Water II Reactor using a CREC-spectroradiometric

606   probe, Chem. Eng. Sci. 116 (2014) 406–417. doi:10.1016/j.ces.2014.04.041.

607   [31] S. Yurdakal, V. Loddo, B.B. Ferrer, G. Palmisano, V. Augugliaro, J.G. Farreras, L. Palmisano,

608   Optical properties of TiO_2 suspensions: Influence of pH and powder concentration on mean

609   particle size, Ind. Eng. Chem. Res. 46 (2007) 7620–7626. doi:10.1021/ie070205h.

610   [32] F. Pellegrino, L. Pellutiè, F. Sordello, C. Minero, E. Ortel, V.D. Hodoroaba, V. Maurino,

611   Influence of agglomeration and aggregation on the photocatalytic activity of TiO_2

612   nanoparticles, Appl. Catal. B Environ. 216 (2017) 80–87. doi:10.1016/j.apcatb.2017.05.046.

613   [33] B. Toepfer, A. Gora, G. Li Puma, Photocatalytic oxidation of multicomponent solutions of

614   herbicides: Reaction kinetics analysis with explicit photon absorption effects, Appl. Catal. B

615   Environ. 68 (2006) 171–180. doi:10.1016/j.apcatb.2006.06.020.

616   [34] J. Colina-Márquez, F. Machuca-Martínez, G. Li Puma, Photocatalytic mineralization of

617   commercial herbicides in a pilot-scale solar CPC reactor: Photoreactor modeling and reaction

618   kinetics constants independent of radiation field, Environ. Sci. Technol. 43 (2009) 8953–8960.

619   doi:10.1021/es902004b.

620   [35]   R.J. Brandi, O.M. Alfano, A.E. Cassano, Rigorous model and experimental verification of the

621   radiation field in a flat-plate solar collector simulator employed for photocatalytic reactions,

622   Chem. Eng. Sci. 54 (1999) 2817–2827. doi:10.1016/S0009-2509(98)00355-8.

623   [36]   J. Hou, Q. Wei, Y. Yang, L. Zhao, Experimental evaluation of scattering phase function and

624   optimization of radiation absorption in solar photocatalytic reactors, Appl. Therm. Eng. 127

625   (2017) 302–311. doi:10.1016/j.applthermaleng.2017.08.046.

626   [37]   R.J. Brandi, M.A. Citroni, O.M. Alfano, A.E. Cassano, Absolute quantum yields in

627   photocatalytic slurry reactors, Chem. Eng. Sci. 58 (2003) 979–985. doi:10.1016/S0009-

628   2509(02)00638-3.

629   [38]   G. Li Puma, A. Brucato, Dimensionless analysis of slurry photocatalytic reactors using two-

630   flux and six-flux radiation absorption-scattering models, Catal. Today. 122 (2007) 78–90.

631   doi:10.1016/j.cattod.2007.01.027.

632   [39]   G. Camera-Roda, V. Augugliaro, A.G. Cardillo, V. Loddo, L. Palmisano, F. Parrino, F.

633   Santarelli, A reaction engineering approach to kinetic analysis of photocatalytic reactions in

634   slurry systems, Catal. Today. 259 (2016) 87–96. doi:10.1016/j.cattod.2015.05.007.

635   [40]   D. Song, Y. Wang, D. Jing, J. Geng, Investigation and prediction of optical properties of

636   alumina nanofluids with different aggregation properties, Int. J. Heat Mass Transf. 96 (2016)

637   430–437. doi:10.1016/j.ijheatmasstransfer.2016.01.049.

638   [41]   D. Jing, D. Song, Optical properties of nanofluids considering particle size distribution:

639   Experimental and theoretical investigations, Renew. Sustain. Energy Rev. 78 (2017) 452–465.

640   doi:10.1016/j.rser.2017.04.084.

641   [42] J.M. Herrmann, Fundamentals and misconceptions in photocatalysis, J. Photochem.

642   Photobiol. A Chem. 216 (2010) 85–93. doi:10.1016/j.jphotochem.2010.05.015.

643   [43] J. Colina-Márquez, F. Machuca-Martínez, G. Li Puma, Radiation absorption and optimization

644   of solar photocatalytic reactors for environmental applications, Environ. Sci. Technol. 44

645   (2010) 5112–5120. doi:10.1021/es100130h.

646   [44] L. Hurtado, R. Natividad, E. Torres-García, J. Farias, G. Li Puma, Correlating the

647   photocatalytic activity and the optical properties of $LiVMoO_6$ photocatalyst under the UV and

648   the visible region of the solar radiation spectrum, Chem. Eng. J. 262 (2015) 1284–1291.

649   doi:10.1016/j.cej.2014.10.052.

650

651

652

653

654

655

656

657

658

659

660

36

661

662

663

664

Supporting Information

Impact of photocatalyst optical properties on the efficiency of

solar photocatalytic reactors rationalized by the concepts of

initial rate of photon absorption (IRPA) dimensionless boundary

layer of photon absorption and apparent optical thickness

Raúl Acosta-Herazo[a], Miguel Ángel Mueses[b]. Fiderman Machuca-Martínez[a], Gianluca Li Puma[c]

[a]*GAOX Research Group, School of Chemical Engineering, Universidad del Valle, A.A. 25360 Cali, Colombia*

[b]*Photocatalysis and Solar Photoreactors Engineering, Department of Chemical Engineering, Universidad de Cartagena, A.A. 1382-Postal 195 Cartagena, Colombia*
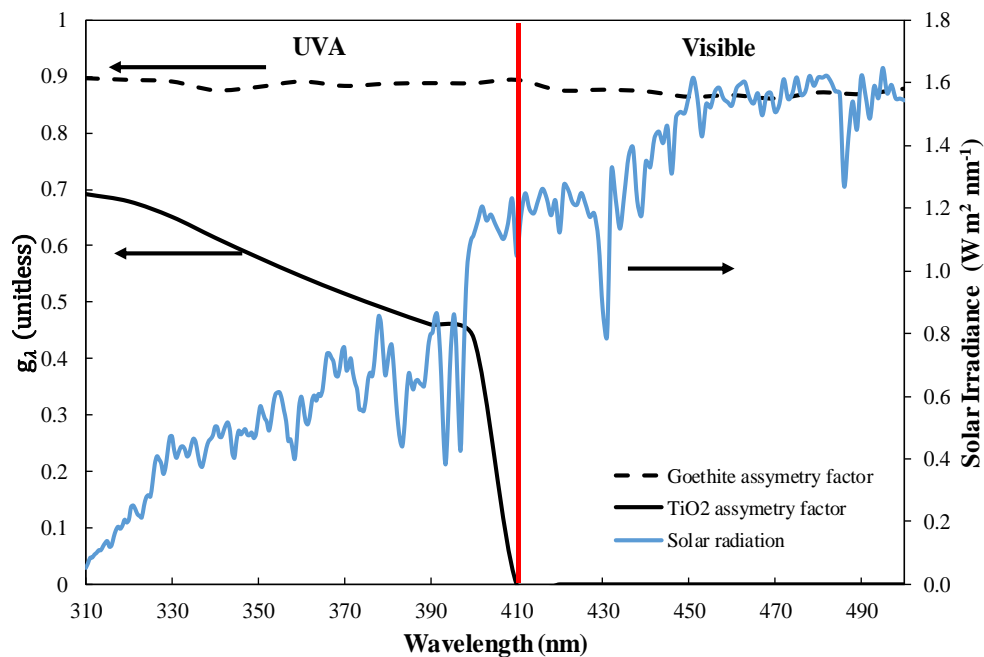
[c]*Environmental Nanocatalysis & Photoreaction Engineering, Department of Chemical Engineering, Loughborough University, Loughborough LE11 3TU, United Kingdom*

679

37

680

Fig. S1 Henyey-Greenstein scattering factor for goethite and TiO$_2$ P25 and solar irradiance for a

surface tilted 37° facing the sun. The red line separates the regions of the solar spectrum. Spectral

data from [19,20]

684
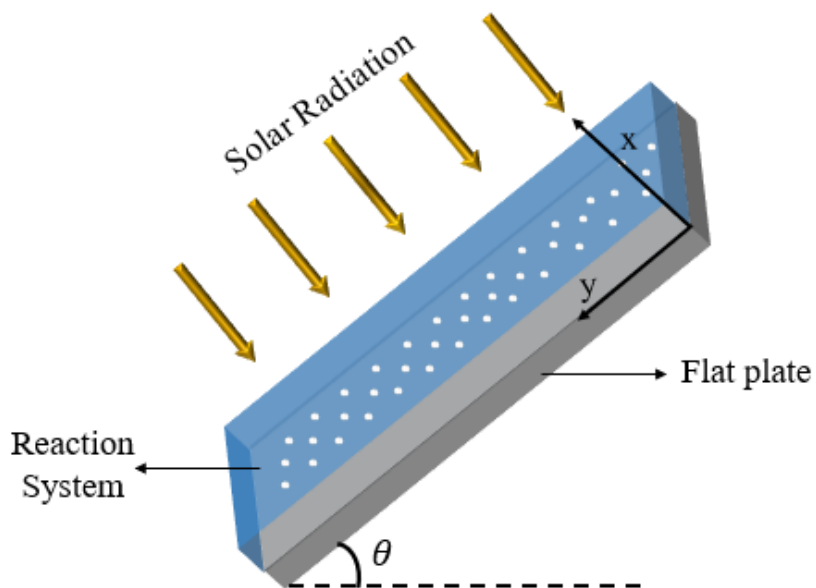
Fig. S2 Model illustration of the planar, slurry photoreactor.

38

686

Table S1. Optical properties of selected visible-active photocatalysts in the visible region of the solar spectrum.

Catalyst	κ^* (m^2/kg)	σ^* (m^2/kg)	ω	Reference
Goethite (Aldrich)	9.52	5.28	0.36	This study
Ag@TiO$_2$	4.7	546.0	0.99	[25]
LiVMoO$_6$	25-26	170-200	0.88[a]	[44]

a. Calculated by the arithmetic average of the κ^* and σ^* reported in the table.

Ttable S2. Fitted quadratic equations to IRPA results in Fig. 5-6.

Catalyst	x-axis data	IRPA quadratic equation	R^2
TiO$_2$	0-0.8 g/L	$8\times10^6 x^2 + 51637x - 30.149$	1
Goethite -UVA	0-30 g/L	$3594x^2 + 0.4733x + 1.4753$	1
Goethite -Visible	0-30 g/L	$2009.9x^2 - 8020x + 7745.7$	1

691

692

693